JGR Space Physics

RESEARCH ARTICLE
10.1029/2020JA028765

Inner Magnetospheric Response to the Interplanetary Magnetic Field B_y Component: Van Allen Probes and Arase Observations

N. A. Case[1], D. P. Hartley[2], A. Grocott[1], Y. Miyoshi[3], A. Matsuoka[4], S. Imajo[3], S. Kurita[5], I. Shinohara[6], and M. Teramoto[7]

[1]Department of Physics, Lancaster University, Lancaster, PA, UK, [2]Department of Physics and Astronomy, University of Iowa, Iowa City, IA, USA, [3]Institute for Space-Earth Environmental Research, Nagoya University, Nagoya, Japan, [4]Graduate School of Science, Kyoto University, Kyoto, Japan, [5]Research Institute for Sustainable Humanosphere, Kyoto University, Kyoto, Japan, [6]Institute of Space and Astronautical Science, JAXA, Sagamihara, Japan, [7]Kyushu Institute of Technology, Kitakyushu, Japan

Key Points:

- The influence of interplanetary magnetic field (IMF) B_y is observed throughout the inner magnetosphere, using Van Allen Probes and Arase observations
- The median ratio of change in the observed B_y to IMF B_y is ~0.33, though a clock angle dependence is found
- We find a consistent effect across both hemispheres, all magnetic local time sectors, and all radial distances

Correspondence to:
N. A. Case,
n.case@lancaster.ac.uk

Citation:
Case, N. A., Hartley, D. P., Grocott, A., Miyoshi, Y., Matsuoka, A., Imajo, S., et al. (2021). Inner magnetospheric response to the interplanetary magnetic field B_y component: Van Allen Probes and Arase observations. *Journal of Geophysical Research: Space Physics*, *126*, e2020JA028765. https://doi.org/10.1029/2020JA028765

Received 6 OCT 2020
Accepted 21 NOV 2020

Abstract We utilize 17 years of combined Van Allen Probes and Arase data to statistically analyze the response of the inner magnetosphere to the orientation of the interplanetary magnetic field (IMF) B_y component. Past studies have demonstrated that the IMF B_y component introduces a similarly oriented B_y component into the magnetosphere. However, these studies have tended to focus on field lines in the magnetotail only reaching as close to the Earth as the geosynchronous orbit. By exploiting data from these inner magnetospheric spacecraft, we have been able to investigate the response at radial distances of $<7R_E$. When subtracting the background magnetic field values, provided by the T01 and IGRF magnetic field models, we find that the IMF B_y component does affect the configuration of the magnetic field lines in the inner magnetosphere. This control is observed throughout the inner magnetosphere, across both hemispheres, all radial distances, and all magnetic local time sectors. The ratio of IMF B_y to the observed B_y residual, also known as the "penetration efficiency," is found to be ~0.33. The IMF B_z component is found to increase, or inhibit, this control depending upon its orientation.

1. Introduction

The presence of a nonzero *y*-component in the interplanetary magnetic field (IMF B_y) has been shown to modify the topology of the magnetic field in the Earth's magnetosphere. First observed by Fairfield (1979), a positive IMF B_y component increases the *y*-component of the background magnetospheric field, while a negative IMF B_y component results in a net decrease.

It has been reported that this effect is not uniform throughout the magnetosphere. Instead, the exact amount by which a nonzero IMF B_y component contributes to the local magnetic field in the magnetosphere has been shown to vary by location, dipole tilt, and the sign of IMF B_z. For example, Fairfield (1979) found an average "penetration efficiency" of the IMF B_y component of 0.13, using data from the IMP-6 spacecraft recorded between $-20R_E$ and $-33R_E$ downtail. That is to say, the change in the local B_y component is 0.13 times the value of the IMF B_y component. Numerous subsequent studies, from different regions of the magnetosphere, have been undertaken showing a broadly similar result but with different penetration efficiencies. For example, both Cowley and Hughes (1983) and Nagai (1987) used data from geostationary satellites (ATS 6 and GOES 6) and found penetration efficiencies of 0.28 and 0.3, respectively. Wing et al. (1995), however, showed that the penetration efficiency at the geosynchronous orbit was much higher, varying between 0.52 and 0.60, depending on whether the data were recorded in the dayside or nightside magnetosphere. A study by Kaymaz et al. (1994), using IMP-8 data, found the "average perturbation" of the local B_y field to be 0.26 times the concurrent IMF B_y strength in the $-25R_E < X_{GSM} \leq 40R_E$ and $|Z_{GSM}| < 8R_E$ regions. Studies from the plasma sheet region of the magnetosphere have observed penetration efficiencies of around 0.50–0.60 (e.g., Lui, 1984; Petrukovich, 2009).

Particularly, with more historical studies, the determination of the background local B_y field value was problematic. In most cases, it was simply determined by using an average of the spacecraft data recorded during geomagnetically "quiet" conditions (i.e., when both the solar wind speed and IMF strength were low). More

recent works utilize sophisticated magnetic field models to determine the background field, for example, Tsyganenko and Andreeva (2020) implemented the radial basis function model of Andreeva and Tsyganenko (2016) to determine the background field. In that work, data from an array of spacecraft missions were compared to determine the effect of IMF B_y at radial distances, $r > 5R_E$. The penetration efficiency was found to depend on both the location and the strength and orientation of IMF B_z.

We note that, despite being widely used in the historical literature, the term "penetration efficiency" is likely inaccurate or, at least, not wholly appropriate. Stemming from earlier studies, such as Cowley (1981), the term implies that the change in the local field topology is a direct result of the IMF field lines themselves making their way, or "penetrating," into the magnetosphere, that is, through the Dungey Cycle (Dungey, 1961). The timescale for this process would be several hours, yet more recent results have suggested that a B_y component can be imparted onto closed field lines over significantly shorter timescales (e.g., Khurana et al., 1996; Tenfjord et al., 2015, 2017), though the issue of timing remains an open question (e.g., Case et al., 2018, 2020). It is for this reason that later studies have tended to refer to the IMF as "inducing" or "transferring" a B_y component onto the magnetospheric field lines—particularly in the region of closed field lines.

In this study, we extend the historical literature to determine the response of the inner magnetosphere ($r < 7R_E$) to the IMF B_y component. To date, the effect of the IMF B_y component on the large-scale local magnetic field in this region, particularly within $5R_E$, has not yet been statistically documented. As described in Section 2, we utilize a multi-mission data set spanning 7 years (17 spacecraft years), as well as an empirically driven magnetic field model, to statistically analyze how the local B_y component changes as a result of the IMF B_y component. In Section 3, we compare the spacecraft measurements, with a model background field subtracted to the IMF B_y for a range of different IMF conditions and find the average "penetration efficiency" to be 0.33 across the entire inner magnetosphere.

2. Data and Methodology

For the purposes of this study, data are used from the Electric and Magnetic Field Instrument Suite and Integrated Science (EMFISIS) fluxgate magnetometer (Kletzing et al., 2013), which is housed onboard the dual satellite NASA Van Allen Probes (formerly Radiation Belt Storm Probe [RBSP]) mission (Mauk et al., 2013). The EMFISIS triaxial fluxgate magnetometer measures the 3D magnetic field vector at a rate of 64 samples per second. This data set is available in full resolution, or with a downsampled cadence of both 1 and 4 s. The following analyses incorporate all available magnetic field observations from both the Van Allen Probes spacecraft spanning the full mission duration, from launch on August 30, 2012, to mission end on October 18, 2019 for RBSP-A, and July 19, 2019 for RBSP-B.

Also included in this study are data from the Japanese geospace exploration project Arase satellite, formerly the exploration of energization and radiation in geospace satellite (ERG) (Miyoshi, Shinohara, et al., 2018b), which was launched on December 20, 2016. The Arase magnetic field experiment (MGF; Matsuoka et al., 2018) measures the magnetic field at a sampling rate of 256 vectors per second, but data are also provided at 64 vectors per second and spin (8 s) resolution. The accuracy of the MGF data is dependent upon which sampling mode the instrument is in, with a lower accuracy for higher dynamic ranges. In this study, we utilize Arase MGF data spanning the period from March 13, 2017 to August 31, 2019, with an accuracy of at least ±1.25 nT. These data are combined with observations from the Van Allen Probes to provide high levels of data coverage across all regions of the inner magnetosphere.

Due to the statistical nature of the following analyses, and to temporally align the spacecraft data with upstream IMF conditions, all spacecraft data are resampled to a 1-min resolution. The IMF data are obtained from the high-resolution (1 min) OMNIweb database (King & Papitashvili, 2005). These data are recorded by several upstream observers and then time-shifted to the bowshock nose. Although there are inherent uncertainties in undertaking such a shifting process, especially when the upstream observer is not close to the Sun–Earth line, the approach is statistically valid (e.g., Case & Wild, 2012; Mailyan et al., 2008). Since we are investigating the magnetic field in the inner magnetosphere, spacecraft data are presented in the solar-magnetic (SM) coordinate system so that they are aligned with the Earth's magnetic dipole. IMF data are presented in the geocentric solar magnetospheric (GSM) coordinate system.

The spatial data coverage of both the Van Allen Probes and Arase missions is provided in Figure 1 in SM coordinates. Data coverage for Van Allen Probes is shown in panels (a and b), Arase in panels (c and d), and the combined data set in panels (e and f). In panels (a, c, and e), data coverage is plotted by location in the X and Y planes, and each bin is $1R_E$ by 1 h in magnetic local time (MLT) in size. In panels (b, d, and f), data coverage is plotted by location in the XY (i.e., $\sqrt{X^2 + Y^2}$) and Z planes, and the bins are $1R_E$ square. The bin fill color represents the total number of 1-min data points contained within it.

For both missions, data coverage is approximately homogeneous in MLT, due to the long duration of the data and the orbital precession of the spacecraft. The greatest number of observations are available between 5 and 6 R_E for both satellite missions, due to their similar apogee altitude. The larger orbital inclination of Arase (31°) provides greater coverage in the Z_{SM} direction than is possible solely from the Van Allen Probes observations (10.2° inclination). We note that the Van Allen Probes mission contributes significantly more data to this study than the Arase mission simply due to its dual-spacecraft nature and longer period of operation.

2.1. Magnetospheric Models

In the following analyses, the Van Allen Probes and Arase in situ magnetic field data are compared against modeled background field values to determine what effect the IMF B_y component has on the magnetic field in the inner magnetosphere. In this region, the background field is a radially dependent combination of an internally driven component (i.e., the terrestrial quasi-dipolar field) and an externally driven component (i.e., the solar wind/IMF-shaped magnetosphere).

To determine the internal component of the background field, we utilize the latest version of the international geomagnetic reference field (IGRF 13) (Thébault et al., 2015). The IGRF is derived from magnetic field data recorded by magnetic observatories, ground surveys, and low Earth orbiting satellites and is regularly updated to account for the latest variations in the Earth's magnetic field. It is independent of any upstream solar wind or IMF conditions.

The externally driven component of the background field is determined using the empirically derived T01 model of the inner magnetosphere (Tsyganenko, 2002a, 2002b). T01 was developed using in situ observations from a range of spacecraft missions (see Figure 1 of Tsyganenko [2002b] for mission and temporal coverage) and is driven by a variety of upstream parameters, including the solar wind speed and the IMF B_y and B_z components, as well as their time history. We note that the Van Allen Probes and Arase missions were not part of the T01 empirical data set and so their data are independent of the modeling data.

The IMF B_y component is utilized as a parameter in the T01 model in the calculation of the IMF clock angle and external magnetic pressure. IMF B_y contributes, for example, to the determination of the model's penetration efficiency term—which is clock-angle-dependent (Equation 10 in Tsyganenko, 2002b). It is therefore expected that the effects of the IMF B_y component on the inner magnetosphere would be hidden when comparing the in situ data with the model output. As such, we also compare the in situ observations with a version of T01 in which we set both the instantaneous and historical IMF B_y to zero. This removes the IMF B_y influence on the modeled B_y field component but ensures that other contributions, such as spacecraft location and dipole tilt angle, are accounted for. We note that the external magnetic pressure exerted on the magnetosphere $\left(\text{i.e.} \frac{B_t^2}{\mu_0}, \text{where } B_t = \sqrt{{B_y}^2 + {B_z}^2} \right)$ will therefore likely be underestimated, however, this is a relatively small systematic offset that does not significantly affect the responses seen (e.g., Tenfjord et al., 2017).

In the subsequent results and discussion, "model" is the modeled field calculated by the addition of the IGRF and T01 field contributions, including IMF B_y as a driver, and $B_{y(\text{mod})}$ is the y-component of this field. "Model*" is the modeled field calculated by the addition of the IGRF and T01, with IMF $B_y = 0$, and $B_{y(\text{mod*})}$ is the y-component of this field. The field measured by the spacecraft is referred to as the "observed" field and $B_{y(\text{obs})}$ denotes the y-component of this field. Although not the primary aim of this study, comparing the "observed" data with "model" allows us to verify that the combination of models we use is working well for our data intervals.

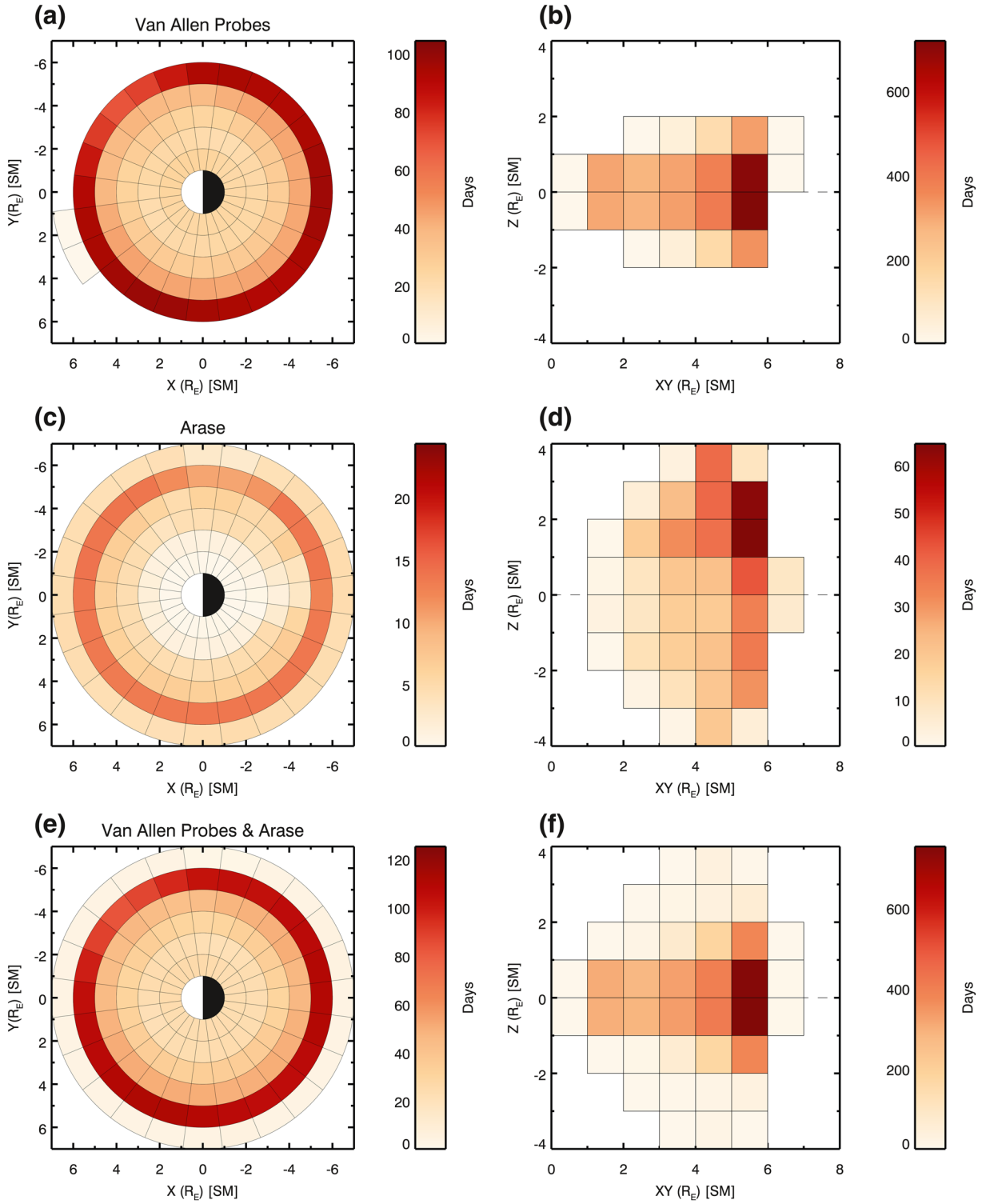

Figure 1. Data coverage for (a and b) Van Allen Probes, (c and d) Arase, and (e and f) both missions combined. Coverage in panels (a, c, and e) is given in the *X*–*Y* plane and bins are $1R_E$ by 1-h MLT in size. In (b, d, and f), coverage is in the *XY*–*Z* plane and bins are $1R_E$ square in size. Bins are colored by the number of 1-min resolution data contained within them (1 day = 1,440 data points). Data are in SM coordinates. MLT, magnetic local time; SM, solar-magnetic.

The spacecraft data are also sorted by hemisphere, i.e., on either side of the neutral sheet which separates the oppositely directed magnetic lobes. Since the neutral sheet is not necessarily located on the $Z_{SM} = 0$ plane, we use both the spacecraft location and the in situ measured field to determine which hemisphere the spacecraft is located in at any given time. Data are defined as being sampled from the Northern Hemisphere when $Z_{SM} > 0\ R_E$ and $B_i < 0$, where $B_i = \left(B_x \cos\theta + B_y \sin\theta\right)$ and $\theta = \tan^{-1}\left(\frac{Y_{SM}}{X_{SM}}\right)$. Conversely, data are defined as being sampled from the Southern Hemisphere when $Z_{SM} < 0\ R_E$ and $B_i > 0$. Given the reasonably steady nature of the solar wind (e.g., Milan et al., 2010), the median IMF B_y is calculated for each spacecraft data point by simply using the preceding 30 min of IMF B_y data, neglecting any propagation time from the bowshock to the magnetopause or magnetospheric response time.

3. Results

Figure 2 shows data recorded in the Northern Hemisphere. In the top row are the median $B_{y(obs)}$ values per bin for (left) IMF $B_y \leq 2$ nT, (center) $|B_y| < 1$ nT, and (right) $B_y > 2$ nT. As with Figure 1, the data bins are $1R_E$ in the radial direction and 1 h in MLT in size. The color of the bin represents the median value.

In the middle row of Figure 2 are the median $B_{y(obs)} - B_{y(mod^*)}$ values. The IMF $B_y \leq 2$ nT panel is clearly dominated by blue colored bins, that is, $B_{y(mod^*)} > B_{y(obs)}$. By contrast, the IMF $B_y > 2$ nT is predominantly red, that is, $B_{y(obs)} > B_{y(mod^*)}$, but with a sizable collection of blue colored bins particularly around the dusk sector. We note too that the IMF $|B_y| < 1$ nT state appears to be dominated by blue bins, suggesting an offset in which model* systematically overestimates the local B_y field. The median absolute relative percentage of the IMF $B_y = 0$ offset to the $B_{y(obs)} - B_{y(mod^*)}$ value for the two nonzero states is 45.0%—though it does vary across MLT and radial distances. To remove this systematic offset, in the bottom row of Figure 2, we plot the median $B_{y(obs)} - B_{y(mod^*)}$ minus the corresponding offset observed for the IMF $|B_y| < 1$ nT state. In both the IMF $B_y > 2$ nT and $B_y \leq 2$ nT cases, the previously mentioned trends become clearer across almost all radial and MLT bins once this offset is removed.

Data recorded in the Southern Hemisphere are plotted in Figure 3, in the same format as in Figure 2. We find a similar response in the Southern Hemisphere as in the Northern Hemisphere, with a clear dependence of the observed B_y component on the IMF B_y component.

MLT sector and hemisphere dependencies are also investigated, with the results shown in Figure 4. Plotted are (panels a and d) the median $B_{y(obs)}$ values, (b and e) median $B_{y(obs)} - B_{y(mod^*)}$, and (c and f) $B_{y(obs)} - B_{y(mod)}$ values as a function of their respective 30 min (a–c) IMF B_y and (d–f) clock angle averages. To determine whether the response of the observed field is different between hemispheres, or between the dusk and dawn sectors, data are separated into the following regions: Northern Hemisphere 01–11 MLT (blue) and 13–23 MLT (red), and Southern Hemisphere 01–11 MLT (green) and 13–23 MLT (orange). The medians of all the regions combined (i.e., all data) are plotted in black. Additionally, for every region, in each panel, a line of the best fit is plotted. For the IMF B_y plots (a–c) the line of best fit is linear, for the clock angle (d–f) plots the line of best fit is a third-order polynomial.

In Figures 4a and 4d, it appears that $B_{y(obs)}$ does not respond to the IMF B_y component. As previously mentioned, however, this is simply because the background field is much larger than the IMF B_y component. When we subtract the background model* field, in panels (b and e), the relationship becomes clear.

As shown in panel (b), there is a clear linear dependence between the IMF B_y component and $B_{y(obs)} - B_{y(mod^*)}$. All MLT regions exhibit a similar response, with the line of best fit equation for all data (black line) being: $B_{y(obs)} - B_{y(mod^*)} = 0.33 \times \text{IMF } B_y - 0.41$ nT. We note that the negative intercept of this line of best fit is consistent with the negative (blue) offset observed in the middle panel of Figure 2.

In Figure 4e, third-order polynomial fits between the IMF clock angle and $B_{y(obs)} - B_{y(mod^*)}$ are shown. Again, these fits are broadly similar for all MLT regions. The turning points of the various fits are all offset from $\theta = \pm 90°$ (i.e., IMF $B_z = 0$). For the all data medians (black line), the maximum and minimum occur at $\theta = 97°$ and $\theta = -109°$ respectively. Both of these turning points demonstrate that while the clock angle must be dominated by the IMF B_y component contribution, it must also contain a rela-

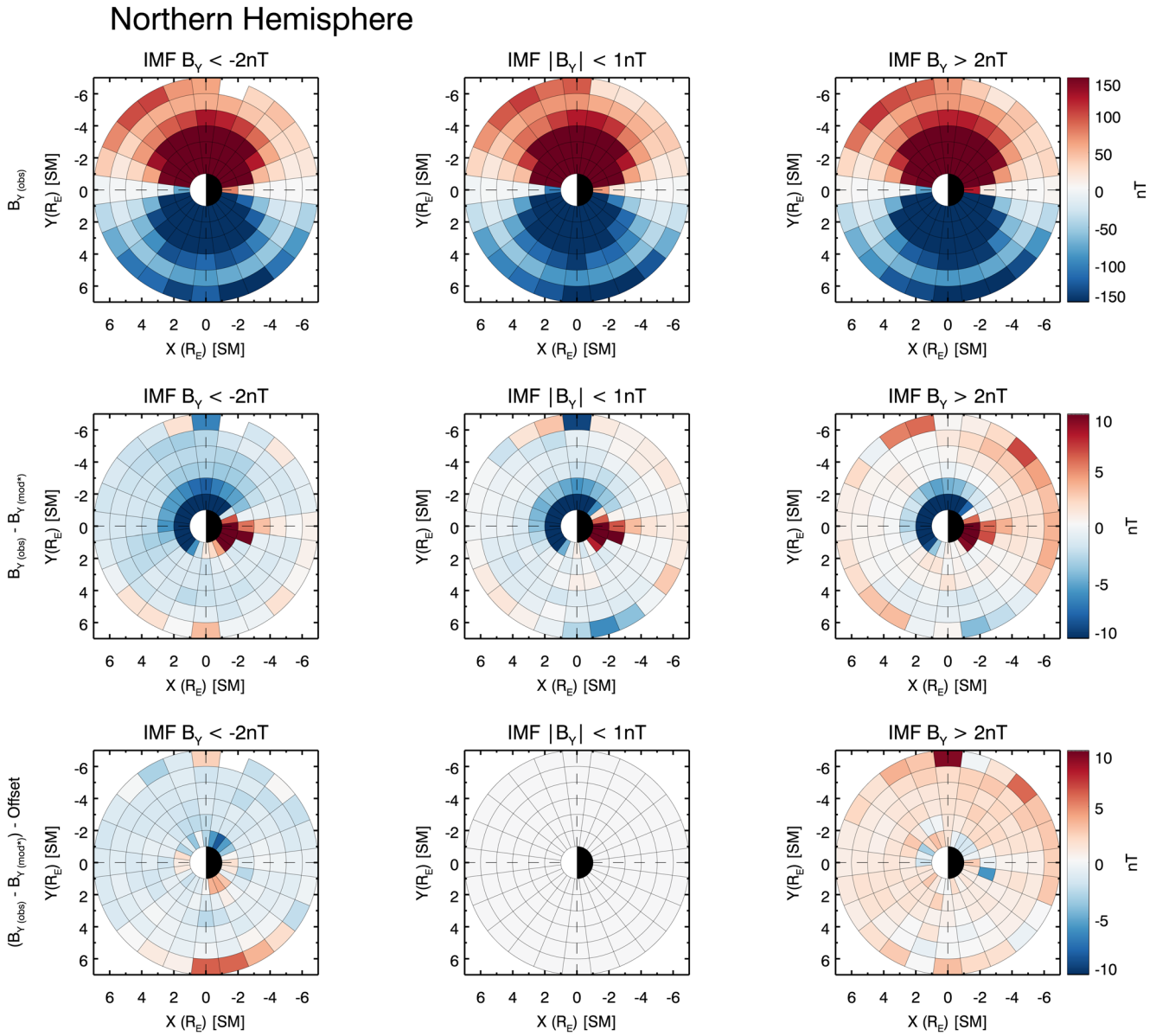

Figure 2. Van Allen Probes and Arase data sampled from the Northern Hemisphere are shown for (left) IMF $B_y \leq 2$ nT, (center) IMF $|B_y| < 1$ nT, and (right) IMF $B_y > 2$ nT states. (Top) Data bins are colored by median local B_y, (middle) the median difference between the local B_y and the modeled B_y value, and (bottom) the median difference between the local B_y and the modeled B_y value with the corresponding median values from the IMF $|B_y| < 1$ state further subtracted. Data bins span $1R_E$ in the radial direction and 1 h in MLT. Abbreviations: IMF: interplanetary magnetic field; MLT, magnetic local time.

tively small southward B_z component to maximize the influence of the IMF B_y component on the inner magnetosphere.

We note that the absolute difference between the maximum and minimum clock angles and $|\theta| = 90°$ is 7 and 19° respectively. This indicates that there is a small asymmetry between the required relative contribution of IMF B_y and B_z for the two IMF B_y orientations. This result suggests that for IMF B_y to be most effective in the inner magnetosphere for $B_y < 0$, a more strongly negative IMF B_z component is required compared with when IMF $B_y > 0$.

In Figures 4c and 4f, $B_{y(\text{obs})} - B_{y(\text{mod})}$ is compared against the IMF B_y component and clock angle. There is no clear trend in either panel that is apparent across all the MLT sectors, and we note that the residuals are small—generally less than 1 nT.

To investigate any radial dependencies in the data, we split the data by the location in MLT and then the bin by the radial distance from the Earth. One representative example of this binning is shown in Figure 5, where data are sampled from the Northern Hemisphere in the 01–11 MLT sector. The lines of best fit plotted in the figure are the medians of the data from this MLT sector, binned by radial distance from the Earth.

The results in Figure 5 are very similar to those in Figure 4. There is a clear linear response at almost all radial distances when $B_{y(obs)} - B_{y(mod^*)}$ is plotted against IMF B_y, and a third-order polynomial response when plotted against the IMF clock angle. In panel (b), the gradients of the IMF B_y linear fits are broadly similar as with the MLT sectors (~0.3). The third-order polynomial fits to the clock angle (panel e) follow similar patterns as before with the maxima and minima, for all fits, occurring at $\theta \sim 95°$ and $\theta \sim -110°$, respectively. We note that the $6 \le r < 7R_E$ bin is an exception to this, which we attribute to the relatively small number of data points in this bin—as is apparent in Figure 1e.

To determine the degree to which the IMF B_y influences the observed B_y component across the whole of the inner magnetosphere, we compute linear lines of best fit for $B_{y(obs)} - B_{y(mod^*)}$, and $B_{y(obs)} - B_{y(mod)}$, as a function of IMF B_y for all MLT-r sectors. The gradients of these fits are plotted in Figure 6. Data are recorded in (a and d) the Northern Hemisphere, (b and e) the Southern Hemisphere, and (c and f) both the hemispheres combined. The gradients of the fits are computed separately for data in each $1R_E$ and 1-h MLT bin. The color of the bins represents the gradient of the fits for the data in that bin. Gray bins indicate limited data (where there was no data for every IMF B_y bin) or poor fits (where the unreduced chi-square goodness-of-fit statistic was greater than 1).

Panels (a–c) show that the fit gradients range from ~0.2 to 0.5 throughout the inner magnetosphere, though there appears to be no particular pattern to this distribution and there is little discernible difference between hemispheres. The gray bins are predominantly due to limited data in the outer radial bins (i.e., $6 \le r < 7R_E$). The result is much more mixed for panels (d–f), with gradients ranging between ±0.2, though again there is no particular pattern to this distribution.

Since Figures 4 and 5 demonstrate that $|B_{y(obs)} - B_{y(mod^*)}|$ is the largest when $|\theta| \sim 90$–$110°$, we have also performed the same analyses as in Figure 6 for two clock-angle-dependent states. Specifically, we plot the distribution of gradients for (a) "all data," (b) $90° < |\theta| \le 135°$, and (c) "other" (i.e., $|\theta| \le 90°$ and $|\theta| > 135°$) in Figure 7.

Figure 7 clearly shows that the distributions for the line of best fit gradients are dependent on the clock angle. The median value is 0.33 for all data, 0.4 for $90° < |\theta| \le 135°$, and 0.3 for "other."

4. Discussion

In this study we have collated magnetic field data from two spacecraft missions in the inner magnetosphere, namely, the Van Allen Probes and Arase. Utilizing the IGRF 13 and T01 magnetic field models to determine the "background field level," we have demonstrated how the IMF B_y component affects the y-component of the magnetic field in the inner magnetosphere.

As shown in Figure 1, our data are recorded in the $R_{XY} < 7R_E$ and $|Z| < 4R_E$ regions, in SM coordinates. The Van Allen Probes and Arase missions provide unparalleled coverage in this region, allowing us to undertake comprehensive statistical analyses of the local magnetic field in the inner magnetosphere with respect to the upstream IMF B_y component.

In the top row of Figure 2, we show the median observed B_y component for three IMF B_y states: IMF $B_y \le 2$ nT, IMF $|B_y| < 1$ nT, and IMF $B_y > 2$ nT. Unsurprisingly, since the total field strength in this region is several orders of magnitude larger than the IMF, there is no discernible difference between the IMF B_y states when the data are presented in this way. However, when the background field ($B_{y(mod^*)}$) is subtracted, as in the middle row of Figures 2 and 3, the response to the IMF B_y component becomes clear. There does, however, appear to be some asymmetry in the data. The IMF $B_y \le 2$ nT shows a much clearer response than the IMF $B_y > 2$ nT state and the IMF $|B_y| < 1$ nT state appears to be more like a weakened version of

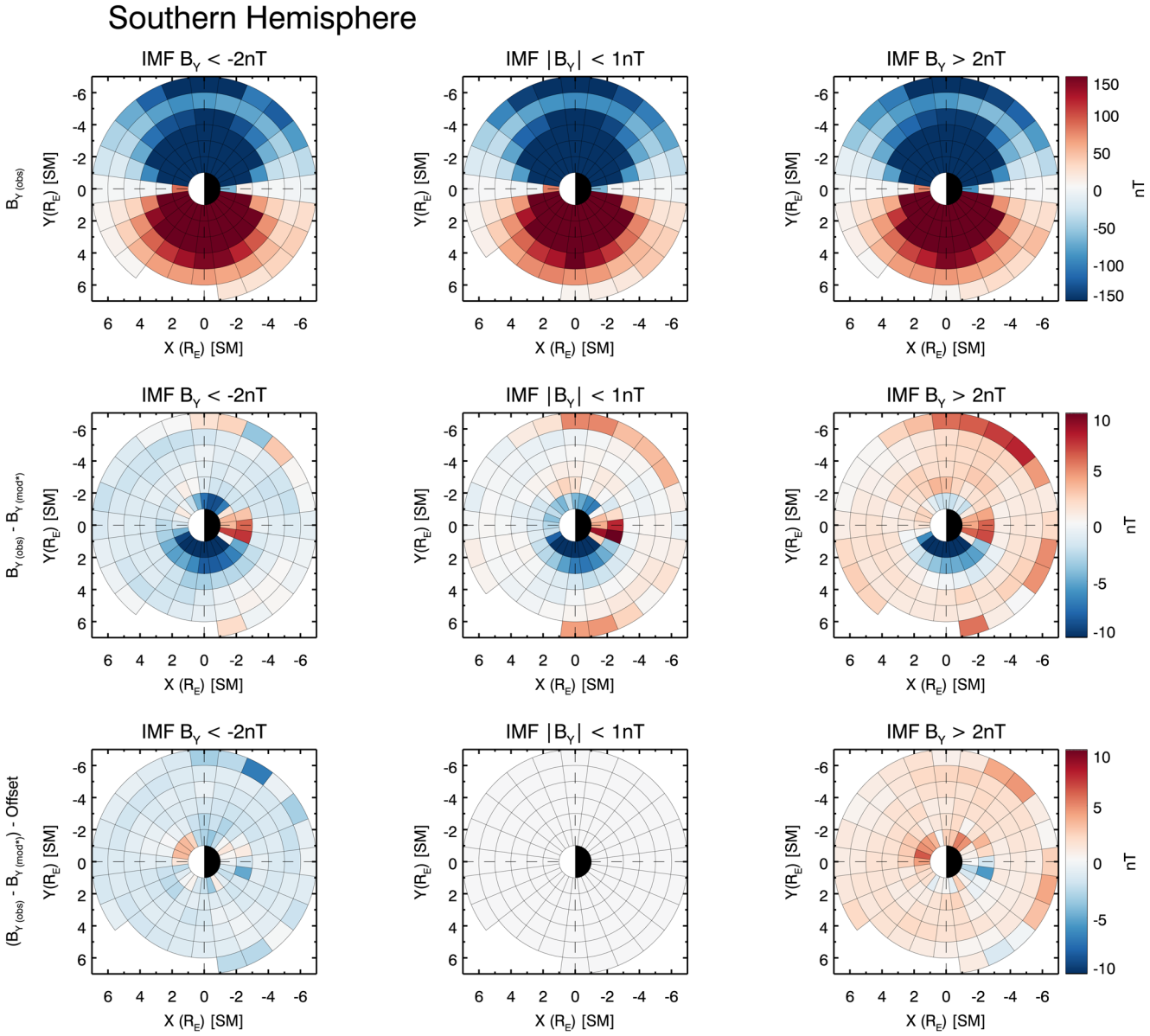

Figure 3. Van Allen Probes and Arase data sampled from the Southern Hemisphere are presented in the same format as in Figure 2.

the IMF $B_y \leq 2$ nT state, rather than a true "neutral" (or zero) state. These results suggest that model* B_y is overestimating the y-component of the magnetic field in all cases. The results from Figure 3 are broadly similar to their counterparts in Figure 2, indicating that there is little-to-no discernible difference between the two hemispheres.

In Figures 4 and 5, we plot the median $B_{y(\mathrm{obs})}$, $B_{y(obs)} - B_{y(mod^*)}$, and $B_{y(\mathrm{obs})} - B_{y(\mathrm{mod})}$ as a function of (a–c) IMF B_y and (d–f) IMF clock angle. In Figure 4, the data are plotted by their location in MLT and in Figure 5 by their radial location. The results of these two figures are similar, and so are discussed together.

In panels (a–c), the data are plotted as a function of IMF B_y in the range of ±6 nT. We note that outside this range the amount of data drops off significantly resulting in poor fits (i.e., a large chi-square goodness-of-fit statistic). Once the background field is subtracted (panel b), the effect of the IMF B_y component becomes clear. Using a linear least squares fit, we find a direct relationship between the IMF B_y and the $B_{y(obs)} - B_{y(mod^*)}$ residual. The gradients, or "penetration efficiencies," are similar for all MLT and r regions,

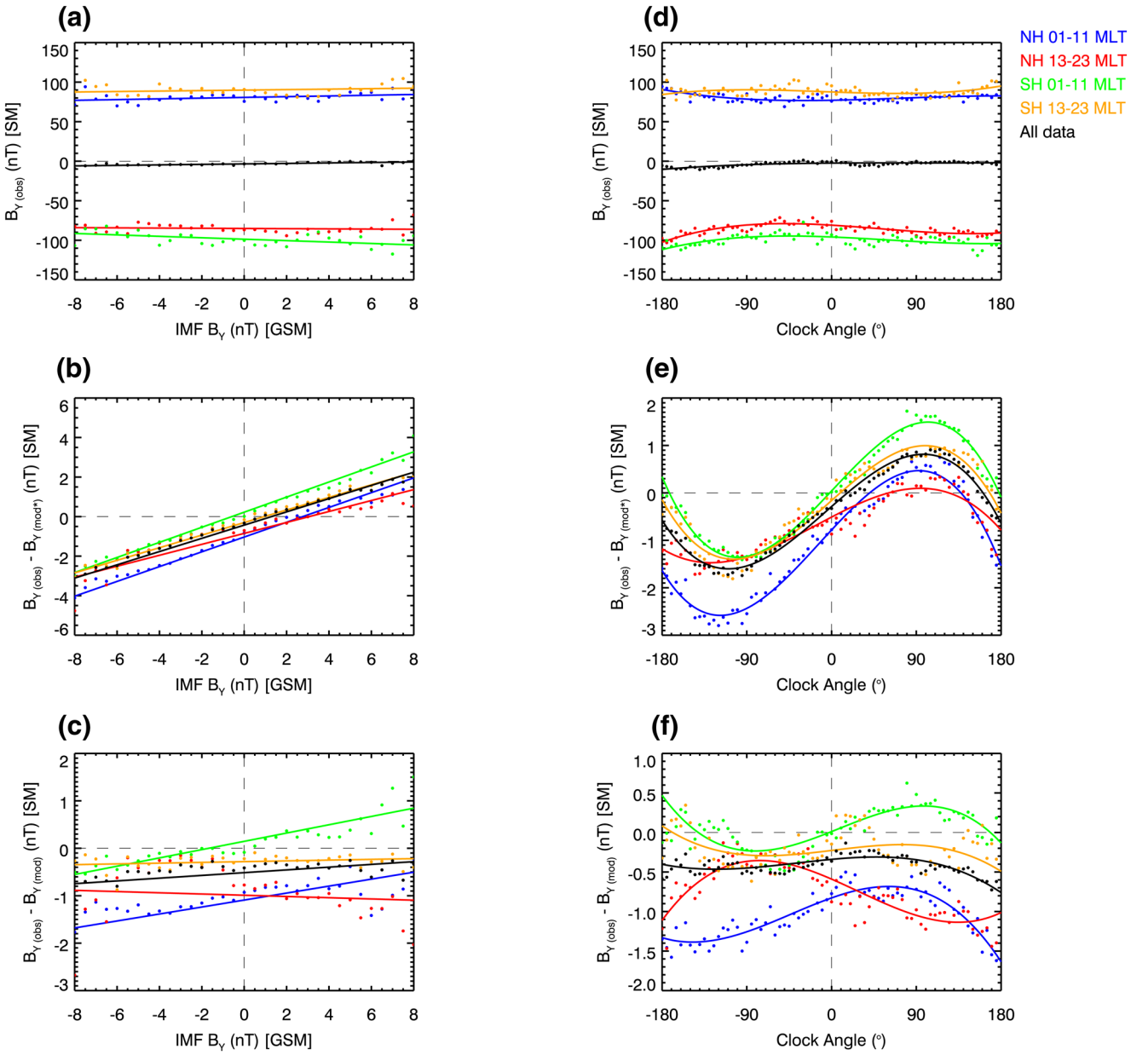

Figure 4. (a) Median $B_{y(\mathrm{obs})}$ values for specific local time and hemispheric sectors, as a function of the upstream IMF B_y and (d) clock angle. (b and e) Medians of the $B_{y(obs)} - B_{y(mod^*)}$ values and (c and f) medians of the $B_{y(obs)} - B_{y(mod)}$ values. In all the panels, the medians from data sampled in the Northern Hemisphere between 01 and 11 MLT are plotted in blue, and between 13 and 23 MLT in red. Medians from data sampled from the Southern Hemisphere between 01 and 11 MLT are plotted in green and between 13 and 23 MLT in orange. The median of all data is plotted in black. IMF, interplanetary magnetic field; MLT, magnetic local time.

averaging around 0.33. While the line of best fit offsets does vary, even the largest offset (Figure 5b) is, when normalized to the strength of the background field, small. Although it is interesting to note that almost all offsets are negative, even when taking into account the IMF B_y component in the model (i.e., $B_{y(\mathrm{obs})} - B_{y(\mathrm{mod})}$)—which is consistent with the slightly negative local B_y state observed for IMF $|B_y| < 1$ nT in Figures 2 and 3.

In Figures 4 and 5d–5f, the data are plotted as a function of the clock angle. Based on the assumption that the fits should have a maximum amplitude when IMF B_y is dominant and zero amplitude when no IMF B_y is present, a third-order polynomial is used to fit the data. A third-order polynomial, unlike a sine

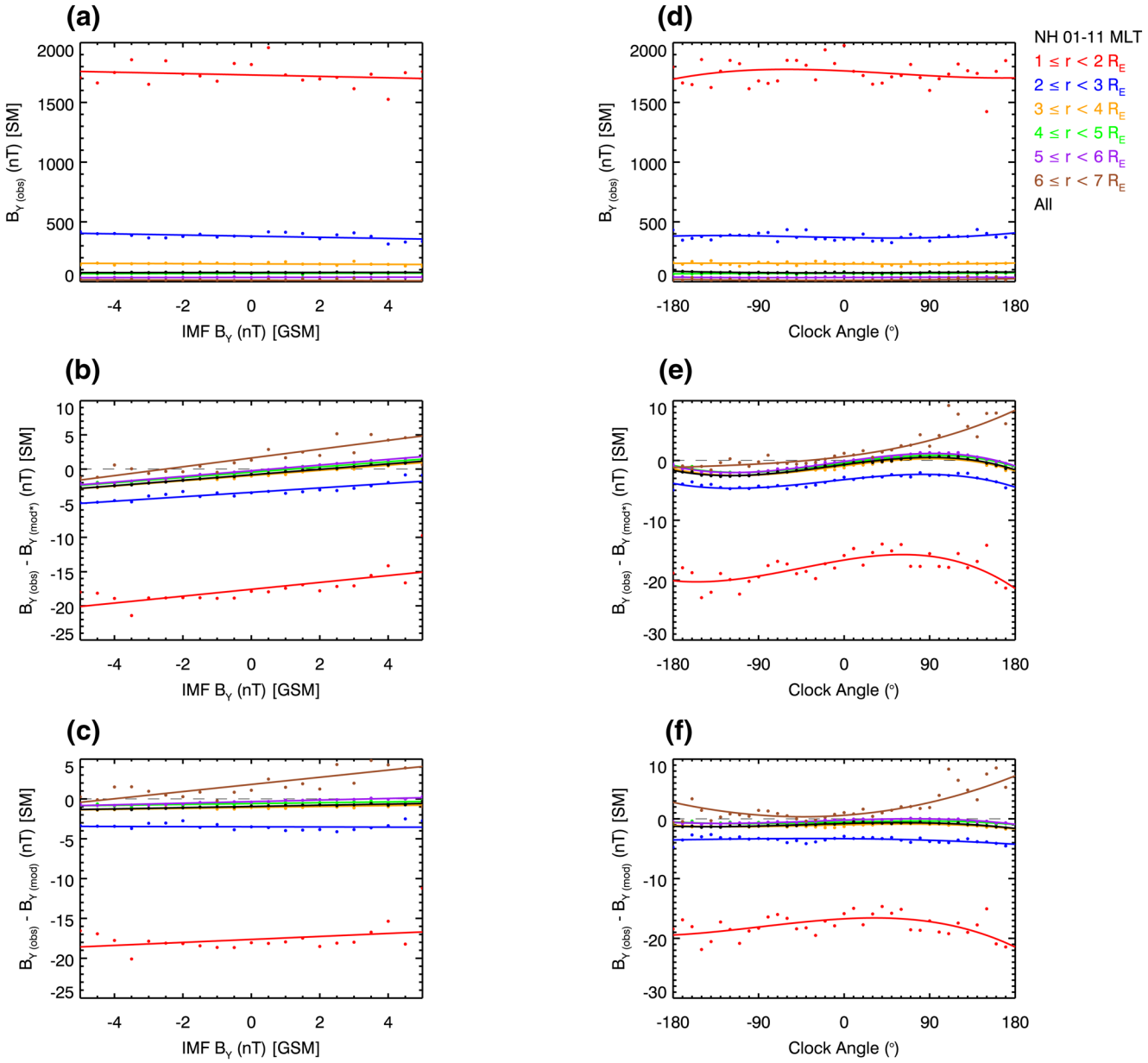

Figure 5. In a similar format as in Figure 4 but with the medians of data by radial distance, for the Northern Hemisphere 01–11 MLT sector, as a function of (a–c) IMF B_y and (d–f) clock angle. IMF, interplanetary magnetic field; MLT, magnetic local time.

function, allows for an asymmetry in the turning points of the fit, which is particularly evident in panel (e) of both the figures. In Figure 4, for example, the maximum turning point is located at $\theta = 97°$ and the minimum turning point at $\theta = -109°$. The clock angles for both the turning points occur when the IMF $|B_y|$ component is several times larger than the IMF $|B_z|$ component, but the IMF B_z component is nonzero and negative. The maximum and minimum of the fits do not occur at the same $|\theta|$, which demonstrates that the ratio between the IMF B_y and B_z components required for the maximum amplitude is different for the two opposite IMF B_y directions. This result may indicate that one orientation of the IMF B_y component more readily facilitates reconnection than the other or that the topology of newly opened flux increases/decreases the efficiency, for which the B_y component is transferred into the inner magnetosphere. We note, however, that these differences are small and are the maximum and minimum of the fits, rather than the data themselves, and so may be prone to fitting error. Further investigation into this observed discrepan-

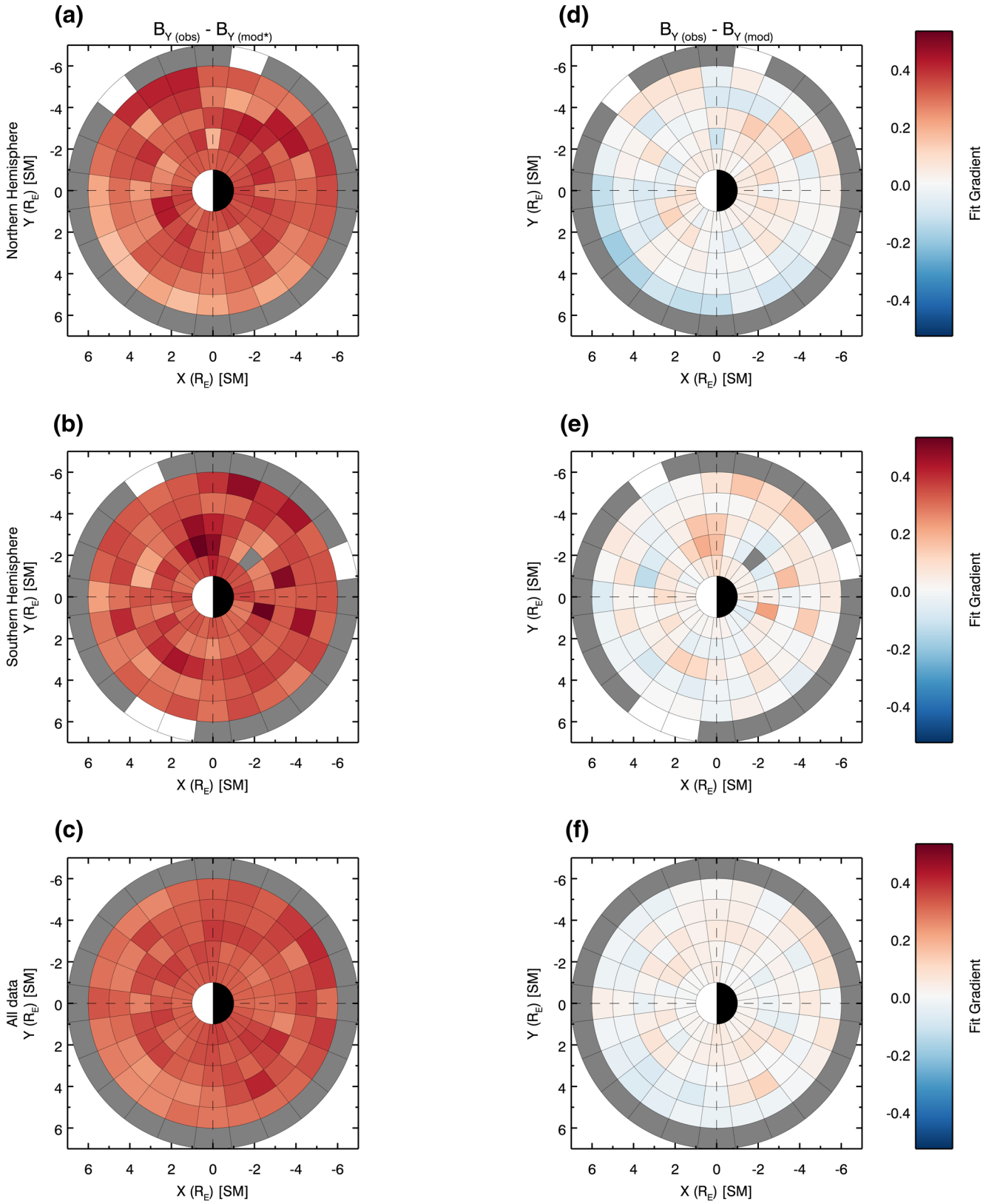

Figure 6. (a–c) Gradients of the linear line of best fits for IMF B_y against $B_{y(obs)} - B_{y(mod^*)}$ and (d–f) for $B_{y(obs)} - B_{y(mod)}$. Data in (a and d) are recorded in the Northern Hemisphere, (b and e) in the Southern Hemisphere, and both hemispheres combined in (c and f). The gradients of the fits are computed for data in $1R_E$ and 1-h MLT bins. The color of the bins represents the gradient of the fits for the data in that bin. Gray bins indicate limited data or poor fits. IMF, interplanetary magnetic field; MLT, magnetic local time.

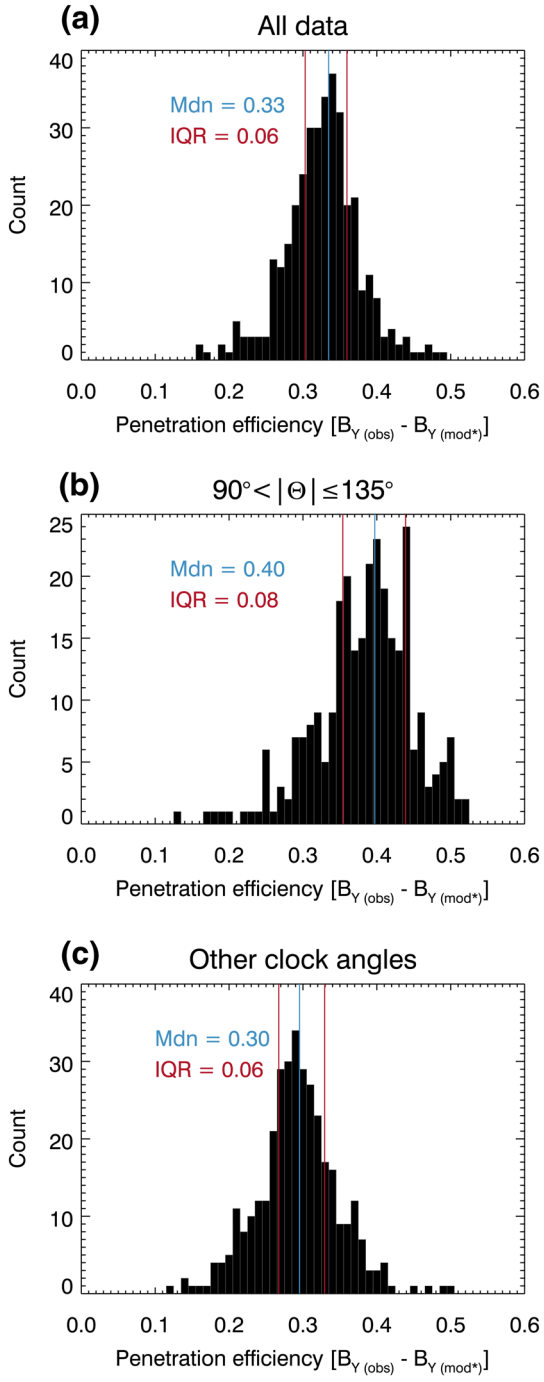

Figure 7. The distribution of linear fit gradients is shown for (a) "all data," (b) 90° < |θ| ≤ 135°, and (c) "other" clock angles. The median and interquartile range are also shown for each distribution.

cy, perhaps through magnetohydrodynamic modeling, therefore seems warranted.

When comparing the hourly averaged IMF and observed B_y components in the $X_{GSM} \sim -20$ to $-30R_E$ regions, Fairfield (1979) found a linear relation of $\Delta B_y(\text{tail}) = 0.13 \times B_y(\text{IMF}) - 0.30$ nT. This compares with our result, as shown in Figure 4 for all data (black line), of $B_{y(obs)} - B_{y(mod^*)} = 0.33 \times \text{IMF}B_y - 0.41$ nT. Of course, our data are recorded in a much different region of the magnetosphere than the IMP 6 spacecraft used by Fairfield (1979) and has also had other non-IMF B_y related effects removed from it through use of the T01 model. Cowley (1981) noted that, because the Fairfield (1979) result was found in both the tail lobes and the plasma sheet, it directly implied the existence of asymmetries on closed field lines. Indeed, all data used in this present study are within $7R_E$, that is, on closed field lines. Numerous studies that followed on from the Fairfield (1979) investigation have found the "penetration efficiency," that is, the gradient of the lines of best fit, to vary depending on the region of the magnetosphere being studied and IMF conditions (e.g., Cao et al., 2014; Cowley & Hughes, 1983; Fairfield, 1979; Lui, 1984; Kaymaz et al., 1994; Nagai, 1987; Petrukovich, 2009; Wing et al., 1995). For example, in the T01 model, which is used throughout this study, the penetration efficiency ranges from 0.068 for northward IMF to 0.622 for southward, however, it is not location dependent (Tsyganenko, 2002b). In recent work by Tsyganenko and Andreeva (2020), modeling of the neighboring regions to that in our study found similar efficiencies of between 0.2 and 0.4, with the larger efficiencies occurring during southward IMF.

The general relationship of $\Delta B_{y(\text{obs})} \sim 0.33 \times \text{IMF}B_y$ holds throughout the inner magnetosphere. There is, of course, some variation in the gradient of the relation by the MLT sector and by radial distance, as can be seen in Figures 4 and 5. However, the median gradient for the 1-h MLT by 1 R_E bins in Figure 6 is 0.33, with an interquartile range of 0.07, suggesting that the general trend holds throughout this region. Again, this is consistent with the recent modeling work, for example, Figure 4 in Tsyganenko and Andreeva (2020).

We note that the southward IMF has resulted in higher penetration efficiency in past studies and, as discussed, we too see this effect in Figures 4e and 5e. We have, therefore, also investigated the effect of the southward IMF on our penetration efficiencies. Shown in Figure 7 are the distributions of the penetration efficiency for three clock angle states: "all data, 90° < |θ| ≤ 135°, and "other." The median penetration efficiencies for these states are 0.33, 0.40, and 0.30, respectively. This result demonstrates that the penetration is higher when the IMF B_y is dominant but accompanied by a negative B_z. This, presumably, is the result of southward IMF driving a larger dayside reconnection rate which, in turn, increases the amount of flux being transferred from the IMF into the magnetosphere. Given that the difference between the median values presented is quite small, we compare the two sample population distributions, using the statistical z-test, finding that the difference between the two distributions is highly significant.

Our analyses have also allowed us to compare the in situ magnetic field with the combined modeling of IGRF 13 and T01. Woodfield et al. (2007) compared T01 with 2 years of perigee Cluster data (~$4R_E$) and found that the model performed very well in a global sense. Although such testing was not the main aim of

this study, our results agree with this assessment. The results of the analyses undertaken, particularly those presented in Figures 4 and 5 (c and f), suggest that the T01 model accurately reflects the impact of the IMF B_y on the observed B_y component in the inner magnetosphere, that is, the line of best fit gradients. Although the offsets of the lines of best fit may sometimes appear large, they represent a small fraction of the total background magnetic field in this region. We note that we are able to attribute this accurate IMF B_y response solely to the T01 model, since the IGRF model does not contain any solar wind/IMF inputs.

In this study, the issue of timing, that is, how long it takes the inner magnetosphere to respond to, and reconfigure based on, the IMF B_y component, has not been investigated. Instead, all spacecraft data were associated with the preceding 30-min average of the IMF B_y component. While the response to the IMF B_y component was clearly seen on this timescale, this does not necessarily mean that it takes 30 min or less for the IMF B_y component to influence the inner magnetosphere. The IMF B_y component tends to have a long auto-correlation length (e.g., Milan et al., 2010) and so the IMF B_y may have been stable for much longer than the averaging period used. Additionally, it does not mean that the system has completely reconfigured in this time, and so we expect our results to include a combination of fully reconfigured states as well as newly responding states. We note the work by Tenfjord et al. (2015, 2017), who found that the inner magnetosphere responded to changes in IMF B_y orientation on timescales of ∼30 min but took longer to fully reconfigure to the new B_y state. Additionally, this was undertaken using GOES data recorded at geosynchronous orbit ($r \sim 6.6R_E$). It would therefore be a worthwhile exercise to investigate the issue of timing using Van Allen Probes and Arase data to determine whether their results hold closer to the Earth. Such future work is planned by the authors.

5. Conclusion

Utilizing 7 years (17 spacecraft years) of data from two spacecraft missions, namely, Van Allen Probes and Arase, we have rigorously investigated the effect of the IMF B_y component on the inner magnetosphere. We have shown that IMF B_y influences the local field in both the hemispheres, all radial distances, and all MLT sectors.

The response of the inner magnetosphere to the IMF B_y component scales linearly in the IMF range analyzed ($-6 \leq$ IMF $B_y \leq +6$ nT). The "penetration efficiency," that is, the fraction of the IMF B_y component that is imparted onto the background inner magnetospheric field is largely consistent throughout the inner magnetosphere at ∼0.33. This result is consistent with previous studies near this region, for example, Tsyganenko and Andreeva (2020).

The penetration efficiency was found to be clock-angle-dependent, specifically the maximum efficiency is observed when the clock angle is dominated by the B_y component but also contains a negative B_z component. Again, this is consistent with previous studies from other regions of the magnetosphere. The median penetration efficiency increased to 0.4 during favorable conditions ($90° < |\theta| \leq 135°$) and dropped to 0.3 during unfavorable conditions.

Additionally, we have found that, in a statistical sense, the Tsyganenko (2002a, 2002b) model, when combined with the IGRF 13 model (Thébault et al., 2015), accounts for the IMF B_y effect well in the inner magnetosphere.

Data Availability Statement

Van Allen Probes EMFISIS data may be obtained from http://emfisis.physics.uiowa.edu/data/index. Science data of the ERG (Arase) satellite were obtained from the ERG Science Center operated by ISAS/JAXA and ISEE/Nagoya University (https://ergsc.isee.nagoya-u.ac.jp/index.shtml.en, Miyoshi, Hori, et al., 2018a). The present study analyzed MGF-L2 v03.03 data (http://doi.org/10.34515/DATA.ERG-06000) and Orbit L3 v02 data. The IGRF 13 and T01 field values were computed using the IDL Geopack DLM (v10.6) (http://ampere.jhuapl.edu/code/idl_geopack.html).

Acknowledgments
The authors gratefully acknowledge both instrument teams for the collection and production of high-quality science data. N. A. Case and A. Grocott were supported during this study by STFC grant number ST/R000816/1. D. P. Hartley performed work under the support of JHU/APL contract number 921647 under NASA Prime contract number NAS5-01072, and JHU/APL contract number 131802 under NASA prime contract number NNN06AA01 C. Y. Miyoshi was supported during this study by JSPS-KAKENHI grants 15H05815, 16H06286, and 20H01959.

References

Andreeva, V. A., & Tsyganenko, N. A. (2016). Reconstructing the magnetosphere from data using radial basis functions. *Journal of Geophysical Research: Space Physics*, *121*(3), 2249–2263. https://doi.org/10.1002/2015JA022242

Cao, J., Duan, A., Dunlop, M., Wei, X., & Cai, C. (2014). Dependence of IMF B_y penetration into the neutral sheet on IMF B_z and geomagnetic activity. *Journal of Geophysical Research: Space Physics*, *119*(7), 5279–5285. https://doi.org/10.1002/2014JA019827

Case, N. A., Grocott, A., Fear, R. C., Haaland, S., & Lane, J. H. (2020). Convection in the magnetosphere-ionosphere system: A multimission survey of its response to IMF by reversals. *Journal of Geophysical Research: Space Physics*, *125*(10). e2019JA027541. https://doi.org/10.1029/2019JA027541

Case, N. A., Grocott, A., Haaland, S., Martin, C., & Nagai, T. (2018). Response of earth's neutral sheet to reversals in the IMF B_y component. *Journal of Geophysical Research: Space Physics*, *123*(10), 8206–8218. https://doi.org/10.1029/2018JA025712

Case, N. A., & Wild, J. A. (2012). A statistical comparison of solar wind propagation delays derived from multispacecraft techniques. *Journal Geophysical Research*, *117*(A2). https://doi.org/10.1029/2011JA016946

Cowley, S. (1981). Magnetospheric asymmetries associated with the Y-component of the IMF. *Planetary and Space Science*, *29*(1), 79–96. https://doi.org/10.1016/0032-0633(81)90141-0

Cowley, S., & Hughes, W. (1983). Observation of an IMF sector effect in the Y magnetic field component at geostationary orbit. *Planetary and Space Science*, *31*(1), 73–90. https://doi.org/10.1016/0032-0633(83)90032-6

Dungey, J. W. (1961). Interplanetary magnetic field and the auroral zones. *Physical Review Letters*, *6*(2), 47–48.

Fairfield, D. H. (1979). On the average configuration of the geomagnetic tail. *Journal of Geophysical Research*, *84*(A5), 1950–1958. https://doi.org/10.1029/JA084iA05p01950

Kaymaz, Z., Siscoe, G. L., Luhmann, J. G., Lepping, R. P., & Russell, C. T. (1994). Interplanetary magnetic field control of magnetotail magnetic field geometry: Imp 8 observations. *Journal of Geophysical Research*, *99*(A6), 11113–11126. https://doi.org/10.1029/94JA00300

Khurana, K. K., Walker, R. J., & Ogino, T. (1996). Magnetospheric convection in the presence of interplanetary magnetic field B_y: A conceptual model and simulations. *Journal of Geophysical Research*, *101*(A3), 4907–4916. https://doi.org/10.1029/95JA03673

King, J. H., & Papitashvili, N. E. (2005). Solar wind spatial scales in and comparisons of hourly Wind and ACE plasma and magnetic field data. *Journal of Geophysical Research*, *110*(A2). https://doi.org/10.1029/2004JA010649

Kletzing, C. A., Kurth, W. S., Acuna, M., MacDowall, R. J., Torbert, R. B., Averkamp, T., & Tyler, J. (2013). The Electric and Magnetic Field Instrument Suite and Integrated Science (EMFISIS) on RBSP. *Space Science Reviews*, *179*, 127–181. https://doi.org/10.1007/s1121401399936

Lui, A. T. Y. (1984). Characteristics of the cross-tail current in the earth's magnetotail. In T. A. Potemra (Ed.), *Magnetospheric currents* (pp. 158–170). American Geophysical Union (AGU). https://doi.org/10.1029/GM028p0158

Mailyan, B., Munteanu, C., & Haaland, S. (2008). What is the best method to calculate the solar wind propagation delay?. *Annales Geophysicae*, *26*(8), 2383–2394. https://doi.org/10.5194/angeo-26-2383-2008

Matsuoka, A., Teramoto, M., Nomura, R., Nosé, M., Fujimoto, A., Tanaka, Y., & Shinohara, I. (2018). The Arase (ERG) magnetic field investigation. *Earth, Planets and Space*, *70*(1), 43. https://doi.org/10.1186/s40623-018-0800-1

Mauk, B. H., Fox, N. J., Kanekal, S. G., Kessel, R. L., Sibeck, D. G., & Ukhorskiy, A. (2013). Science objectives and rationale for the Radiation Belt Storm Probes mission. *Space Science Reviews*, *179*(1), 3–27. https://doi.org/10.1007/s11214-012-9908-y

Milan, S. E., Grocott, A., & Hubert, B. (2010). A superposed epoch analysis of auroral evolution during substorms: Local time of onset region. *Journal of Geophysical Research*, *115*(A5). https://doi.org/10.1029/2010JA015663

Miyoshi, Y., Hori, T., Shoji, M., Teramoto, M., Chang, T. F., Matsuda, S., & Shinohara, I. (2018a). The ERG science center. *Earth, Planets and Space*, *70*, 96. https://doi.org/10.1186/s40623-018-0867-8

Miyoshi, Y., Shinohara, I., Takashima, T., Asamura, K., Higashio, N., Mitani, T., & Seki, K. (2018b). Geospace exploration project ERG. *Earth, Planets and Space*, *70*(1), 101. https://doi.org/10.1186/s40623-018-0862-0

Nagai, T. (1987). Interplanetary magnetic field by effects on the magnetic field at synchronous orbit. *Journal of Geophysical Research*, *92*(A10), 11215–11220. https://doi.org/10.1029/JA092iA10p11215

Petrukovich, A. A. (2009). Dipole tilt effects in plasma sheet B_y: statistical model and extreme values. *Annales Geophysicae*, *27*(3), 1343–1352. https://doi.org/10.5194/angeo-27-1343-2009

Tenfjord, P., Østgaard, N., Snekvik, K., Laundal, K. M., Reistad, J. P., Haaland, S., & Milan, S. E. (2015). How the IMF B_y induces a B_y component in the closed magnetosphere and how it leads to asymmetric currents and convection patterns in the two hemispheres. *Journal of Geophysical Research: Space Physics*, *120*(11), 9368–9384. https://doi.org/10.1002/2015JA021579

Tenfjord, P., Østgaard, N., Strangeway, R., Haaland, S., Snekvik, K., Laundal, K. M., & Milan, S. E. (2017). Magnetospheric response and reconfiguration times following IMF B_y reversals. *Journal of Geophysical Research: Space Physics*, *122*(1), 417–431. https://doi.org/10.1002/2016JA023018

Thébault, E., Finlay, C. C., Beggan, C. D., Alken, P., Aubert, J., Barrois, O., & Zvereva, T. (2015). International geomagnetic reference field: The 12th generation. *Earth, Planets and Space*, *67*(79). https://doi.org/10.1186/s40623-015-0228-9

Tsyganenko, N. A. (2002). A model of the near magnetosphere with a dawn-dusk asymmetry 1. Mathematical structure. *Journal of Geophysical Research*, *107*(A8), SMP12-1–SMP12-15. https://doi.org/10.1029/2001JA000219

Tsyganenko, N. A. (2002). A model of the near magnetosphere with a dawn-dusk asymmetry 2. Parameterization and fitting to observations. *Journal of Geophysical Research*, *107*(A8), SMP10-1–SMP10-17. https://doi.org/10.1029/2001JA000220

Tsyganenko, N. A., & Andreeva, V. A. (2020). Magnetospheric "penetration" of IMF viewed through the lens of an empirical RBF modeling. *Journal of Geophysical Research: Space Physics*, *125*(1). e2019JA027439. https://doi.org/10.1029/2019JA027439

Wing, S., Newell, P. T., Sibeck, D. G., & Baker, K. B. (1995). A large statistical study of the entry of interplanetary magnetic field y-component into the magnetosphere. *Geophysical Research Letters*, *22*(16), 2083–2086. https://doi.org/10.1029/95GL02261

Woodfield, E. E., Dunlop, M. W., Holme, R., Davies, J. A., & Hapgood, M. A. (2007). A comparison of cluster magnetic data with the tsyganenko 2001 model. *Journal of Geophysical Research*, *112*(A6). https://doi.org/10.1029/2006JA012217